Electromagnetic Field Absorbing Polypropylene Nanocomposites with Tuned Permittivity and Permeability by Nanoiron and Carbon Nanotubes

Qingliang He,[†,‡,▽] Tingting Yuan,[†] Xi Zhang,[†] Xingru Yan,[†] Jiang Guo,[†] Daowei Ding,[†] Mojammel A. Khan,[‖] David P. Young,[‖] Airat Khasanov,[⊥] Zhiping Luo,[#] Jiurong Liu,*,[%] T. D. Shen,[$] Xinyu Liu,[§] Suying Wei,*,[‡] and Zhanhu Guo*,[†,▽]

[†]Integrated Composites Laboratory (ICL), Dan F. Smith Department of Chemical Engineering, [‡]Department of Chemistry and Biochemistry, and [§]Department of Industrial Engineering, Lamar University, Beaumont, Texas 77710, United States

[‖]Department of Physics and Astronomy, Louisiana State University, Baton Rouge, Louisiana 70803, United States

[⊥]Department of Chemistry, University of North Carolina at Asheville, Asheville, North Carolina 28804, United States

[#]Department of Chemistry and Physics, Fayetteville State University, Fayetteville, North Carolina 28301, United States

[%]Key Laboratory for Liquid—Solid Structural Evolution and Processing of Materials, Ministry of Education and School of Materials Science and Engineering, Shandong University, Jinan, Shandong 250061, P. R. China

[$]State Key Laboratory of Metastable Materials Science and Technology, Yanshan University, Qinhuangdao 066004, P. R. China

[▽]Engineered Multifunctional Composites, LLC, Beaumont, Texas 77713, United States

ABSTRACT: Highly efficient electromagnetic field absorption at gigahertz (GHz) was reported in the novel magnetic polymer nanocomposites (MPNCs) with in-situ synthesized $Fe@Fe_2O_3$ core@shell nanoparticles (NPs) or their decorated multiwall carbon nanotubes (MWNTs) dispersed in the polypropylene (PP) matrix through a one-pot bottom-up method. PP grafted maleic anhydride (PP-g-MA) with different molecular weights served as surfactant to stabilize the in-situ-formed NPs and simultaneously as compatibilizer to enhance the bonding at the PP—filler interfaces. Because of the strong magnetization of the PP MPNCs filled with 20.0 wt % $Fe@Fe_2O_3$ NPs stabilized by PP-g-MA (M_n = 800), a minimum reflection loss (RL) of −31.5 dB was observed at 18.0 GHz, and the frequency bandwidth with RL lower than −10.0 dB was 3.1 GHz (from 16.9 to 20.0 GHz) in the MPNC sample with a thickness of 5.5 mm. However, due to the lack of magnetic loss, only a weak RL of 4.3 dB was found at frequency of 16.8 GHz for the PP/PP-g-MA (M_n = 800)/1.0 wt % MWNTs nanocomposites sample with a thickness of 5.5 mm. When the PP MPNCs filled with $Fe@Fe_2O_3$ NPs decorated MWNTs (sample thickness of 5.0 mm) in the presence of low molecular weight PP-g-MA (M_n = 800), the RL of −24.5 dB at 20.0 GHz was observed. Through simply changing M_n of PP-g-MA from 800 to 8000, more oxidized iron resulted in a decreased permeability and smaller RL in the high frequency range. The in-situ-formed nanofillers significantly reduced the flammability of PP for potential wide applications.
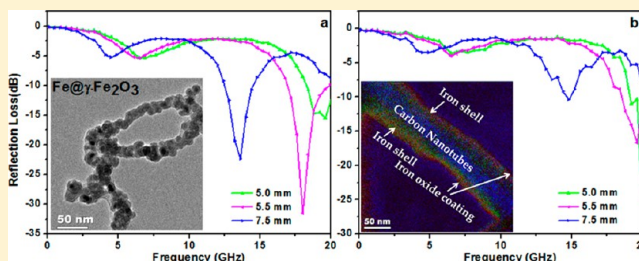
1. INTRODUCTION

Electromagnetic interference (EMI) is an undesirable and uncontrolled offshoot of both the explosive growth of electronics such as wireless cell phones with gigahertz (GHz) high energy ($E = hf$, where h is Planck's constant and f is frequency) EM field and the widespread use of transient power sources.[1,2] Human beings raised concerns over exposure to EM radiation in our modern lives.[3,4] Embedding magnetic nano/microstructures into polymer matrix for EM wave absorption is one of the most effective approaches for EMI shielding.[5,6] Theoretically, magnetic nanostructures such as iron nanoparticles (NPs) can provide high absorption over a wide frequency range as a result of their high magnetization,[7,8] high Snoek's limit, and quantum size effect.[9] Magnetic NPs are ideal to serve as EM absorbers because of their small size[10] and large

specific surface area,[11] leading to an interface polarization[12] and effective usage of active metals.[13] However, high frequency (i.e., in GHz range) permeability of the metallic magnetic materials can be drastically decreased due to the ferromagnetic resonance[14,15] and eddy-current losses (a source of energy loss in alternating current inductors, etc.) induced by the EM wave.[16,17] The decreased permeability will significantly reduce the EM wave absorption efficiency at GHz. For example, dendritic nanostructured α-iron (Fe) in paraffin was reported with a minimum reflection loss (RL) of 32.3 dB at ~10.0 GHz at a relatively high loading (70 wt %).[18] The reason for such a

strong EM wave absorption is explained by the high-frequency resonance derived from large coercive field (H_c, larger than 200 Oe) of the dendritic nanostructure.[18] Even though high response frequency of minimum RL value was observed, the increased permittivity and the relatively low dielectric loss are the major drawbacks for the metallic iron as EM absorbers at even higher frequency.

Another type of EM wave absorption material is the polymer composites filled with carbon-based nanofillers.[19−26] For example, strong microwave absorbing intensities of −64.4 dB at 10.59 GHz were reported in the poly(vinylidene fluoride) (PVDF)−graphite intercalated composites (GIC).[27] However, the filler loading of 9.0 wt % was relatively high, which inevitably increased the permittivity. It is well acknowledged that the dielectric permittivity and magnetic permeability are typically out of balance for the polymer composites with carbon-based nanofillers,[28] a high propensity to reflect rather than absorb the EM wave would be a major drawback arising from the lack of magnetic loss in these carbon materials. Though carbon materials like graphene in polymer foam matrix are reported to absorb rather than reflect EM wave,[24] high absorption effectiveness lower than −20 dB with a wide frequency range is still a challenge.[22,24,29] Therefore, the combination of magnetic and dielectric materials in one unit is desirable for highly effective EM field absorption in a broad frequency range with controllable permittivity and permeability matched with those of free space.[6,28,30] For example, carbon nanotubes (CNTs) decorated with magnetite (Fe_3O_4) particles[31−33] and reduced graphene oxide decorated with Fe_2O_3 or Fe_3O_4 NPs[34−36] have demonstrated an enhanced EM absorption. In addition, Fe_3O_4-coated carbon nanorods show a strong dielectric loss at high-frequency range and strong magnetic loss at low-frequency range.[37] However, impendence mismatch remains as the major hindrance for effective EM wave absorption. For example, iron confined in CNTs displayed an enhanced EM absorption (lower than −25.0 dB RL at a frequency of ∼11.0 GHz) mainly arising from the magnetic rather than dielectric loss.[38]

The reported methods to prepare hierarchical nanostructures include direct blending,[6] coprecipitation,[36] and solvothermal method.[39] Besides, the bottom-up wet chemistry method is one of the most powerful approaches to synthesize different nanostructures including magnetic NPs with well-defined dispersion quality and assembly patterns with the aid of small molecular surfactants.[40−43] Physical mixing,[6,34,36,39,44,45] and emulsion polymerization[35] have been reported to disperse those aforementioned ex-situ-formed hierarchical nanostructures in the polymer matrix to prepare EM wave absorbing polymer composites. Though the majority of the above works are to synthesize EM absorbing polymer composites through the ex-situ method, magnetic polymer nanocomposites (MPNCs) with one-pot in-situ-formed hierarchical nanofiller architectures (combining both magnetic and carbon materials) have not been reported yet. Herein, in this work, a facile one-pot in-situ method was reported to prepare polypropylene (PP) MPNCs filled with both $Fe@Fe_2O_3$ core−shell NPs and multiwall carbon nanotubes (MWNTs) decorated with $Fe@Fe_2O_3$ NPs in the presence of PP grafted maleic anhydride (PP-*g*-MA). The EM field absorption of these MPNCs was evaluated by the reflection loss considering the relative permeability and permittivity. The hierarchical magnetic NPs decorated MWNTs for EM wave absorption behaviors was studied and compared with the sole magnetic NPs and

MWNTs. Meanwhile, the surfactant molecular weight dependent frequency selective EM wave absorption performance was demonstrated by using two different molecular weight PP-*g*-MAs. In addition, the flammability of these MPNCs was evaluated by microscale combustion calorimetry.

2. EXPERIMENTAL SECTION

2.1. Materials. The PP used in this study was supplied by Total Petrochemicals USA, Inc. ($M_n \approx 40\,500$). Two PP-*g*-MAs (provided by Baker Hughes Inc.) were utilized. The first of PP-*g*-MA ($M_n = 800$, denoted as "S") was a gel-like copolymer with one maleic anhydride (MA) group at one terminal through the Alder−ENE reaction[46] and the other MA group grafted on the main chain. The second of PP-*g*-MA ($M_n = 8000$, denoted as "L") was solid homo-PP with two MA groups (structures shown in Scheme 1). Iron(0) pentacarbonyl ($Fe(CO)_5$, 99%)

Scheme 1. Chemical Structures of PP-*g*-MA, S, and L

PP-g-MA-S, M$_n$=800   **PP-g-MA-L, M$_n$=8000**
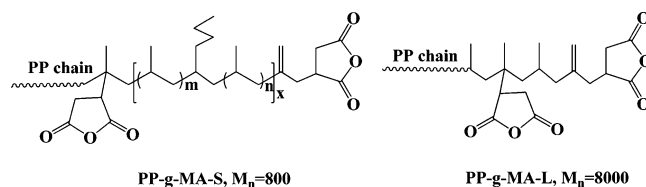
was purchased from Sigma-Aldrich. The multiwall carbon nanotubes (MWNTs) used here were COOH-functionalized tubes (−COOH content: 0.47−0.51 wt %; purity: >95%; average outer diameter of 50−80 nm, inner diameter of 5−15 nm, and length of 10−20 μm) supplied by Nanostructured and Amorphous Materials, Inc., Houston, TX. The solvent xylene (laboratory grade, $\rho = 0.87$ g/cm^3) was purchased from Fisher Scientific. All the chemicals were used as-received without any further treatment.

2.2. Synthesis of Polymer Nanocomposites. The brief procedures for preparing the PP MPNCs with in-situ-formed hierarchical nanostructures (MWNTs decorated with Fe@Fe_2O_3 NPs) are as follows. The PP pellets (7.4 g) and 100 mL of xylene added into a 500 mL three-neck round-bottom flask were heated to reflux at ∼140 °C in order to dissolve PP. At the same time, 0.5 g of PP-*g*-MA (type "S" or "L") was dissolved in 20 mL of xylene in a 100 mL beaker under ∼140 °C, in which 0.1 g of MWNTs was added. The mixture was further placed in the ultrasonication bath for 1 h to form a colloidal solution. The MWNTs/PP-*g*-MA mixture solution was transferred into the flask, which was heated to reflux and then cooled down to around 120 °C. Then, 7.0 g of $Fe(CO)_5$ was injected into the flask to obtain a 20.0 wt % Fe-PP MPNCs (calculation was based on pure Fe element weight fraction). The solution immediately turned from transparent to brown and then gradually black during refluxing for an additional 4 h at 140 °C. The reflux speed was controlled at approximately 1−2 drops/s to maintain a smooth reaction. Finally, the solution was cooled down to room temperature and then poured into a large glass container to evaporate solvent in the fume hood. The black powders were then dried in a vacuum oven at room temperature. The PP/20.0 wt % Fe MPNCs (7.5 g of PP, 0.5 g of PP-g-MA (S), and 7.0 g of $Fe(CO)_5$ without MWNTs), and PP/5.0 wt % PP-g-MA/1.0 wt % MWNTs composites were also prepared as control using the same procedures. The Fe loading was fixed at 20.0 wt % for all the MPNCs, and the
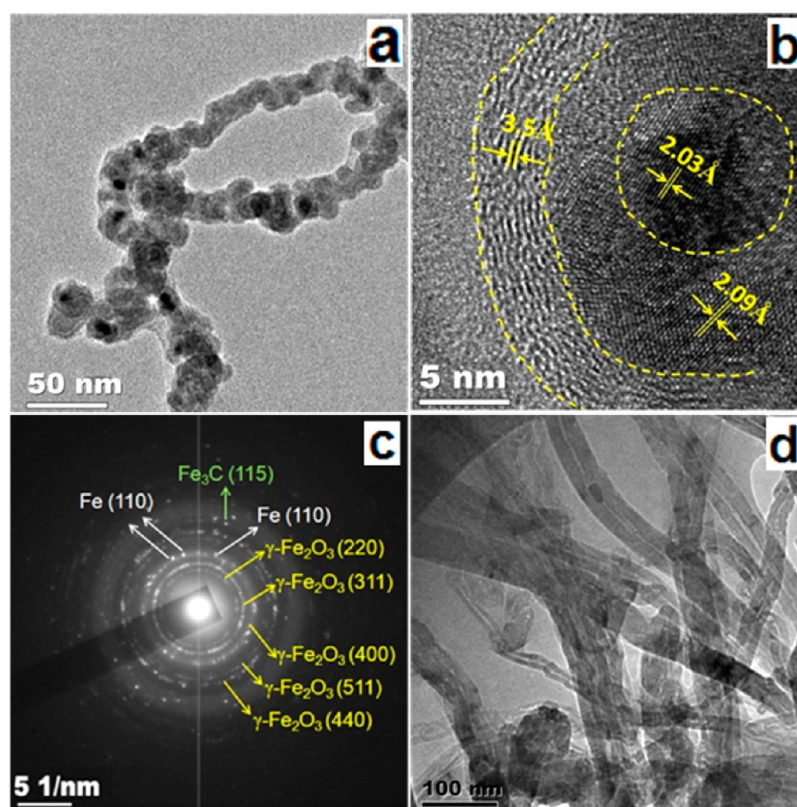
Figure 1. (a) TEM, (b) HRTEM images, (c) SAED pattern of PP/5.0% PP-*g*-MA(S)/20.0% Fe MPNCs, and (d) TEM image of the PP/5.0% PP-*g*-MA(S)/1.0% MWNTs PNCs.

loading of MWNTs was 1.0 wt % except the one without MWNTs.

The desired samples were prepared from the final powders using a hot press molding machine (Carver 3853-0). The concise procedures were as follows. The powders were added into a cylinder-shaped mold, which was placed between the two panels in the molding machine. The mold was then heated to 180 °C at a heating rate of 20 °C/min under a pressure of 10 MPa and maintained at 180 °C for 5−10 min to ensure the formation of compact samples. Finally, the sample was cooled down naturally to room temperature in the mold.

2.3. Characterization. A transmission electron microscope (TEM) was used to characterize the particle morphology of the as-prepared PP MPNCs in a FEI TECNAI G2 F20 microscope at a working voltage of 200 kV. The samples were prepared from the hot solution of the PP MPNCs at the end of synthesis process. One droplet of the diluted hot solution containing NPs was dropped on a 400-mesh carbon-coated copper grid (Electron Microscopy Sciences). The average particle size was measured by software named "Nano Measurer" based on approximately 60−100 particles in the obtained TEM images.

Scanning electron microscopy (SEM, JEOL JSM 6700R in high-vacuum mode) was further utilized to demonstrate the dispersion of the NPs in the PP matrix in the presence/absence of PP-*g*-MA. The samples were mounted on an aluminum stub by using carbon tape. Then, the samples were sputtered (Hummer 6.2 system, 15 mA AC for 30 s) to form approximately 1 nm thick film of Au for better imaging. X-ray diffraction (XRD) analysis was carried out with a Bruker AXS D8 Discover diffractometer operating with a Cu K*α* radiation source. The XRD patterns were recorded at 2*θ* from 5° to 70°.

The Mössbauer spectrometer was set to produce a high precision Doppler velocity modulation of the source *γ* radiation. The effects of the Doppler velocity modulation on the absorption of *γ* radiation were recorded synchronously in the 1024 channels of the multichannel analyzer. The result was 1024 numbers representing registered gamma quanta (representing a singular quantum) passing through the absorber under the condition of different Doppler velocity. A separate calibration procedure was used to establish the exact correspondence channel velocity. (Spectrometer calibration was performed by measuring a standard *α*-Fe absorber, which produces a well-known six-line spectrum. The whole velocity range was calibrated using these six velocity points.) The shape of the absorption spectrum was fitted to a theoretical model line shape, which was a superposition of singlets, doublets, and sextets (^{57}Fe case) of a Lorentzian form. The result was investigated by chi^2 criterion, and the theoretical line shape was tailored to fit experimental spectrum by the adjustment of spectral parameters like isomer shift, quadrupole splitting, hyperfine magnetic field, etc.

The magnetic property measurements of all the PP MPNCs were carried out in a 9 T physical properties measurement system (PPMS) by Quantum Design at room temperature.

The relative complex permeability ($\mu = \mu' + \mu''$) and permittivity ($\varepsilon = \varepsilon' + \varepsilon''$) were measured using a network analyzer (Agilent Technologies model N5232A) based on the transmission line technique. A donut-shaped specimen was cut from the as-prepared composite thin sheet (∼2.5 mm) after hot press. The outer and inner diameters of the specimen were 7.00 and 3.04 mm, respectively. The specimen was polished by a 320-grit SiC abrasive paper on a granite flat until a smooth and uniform surface was achieved. The specimen was then placed in
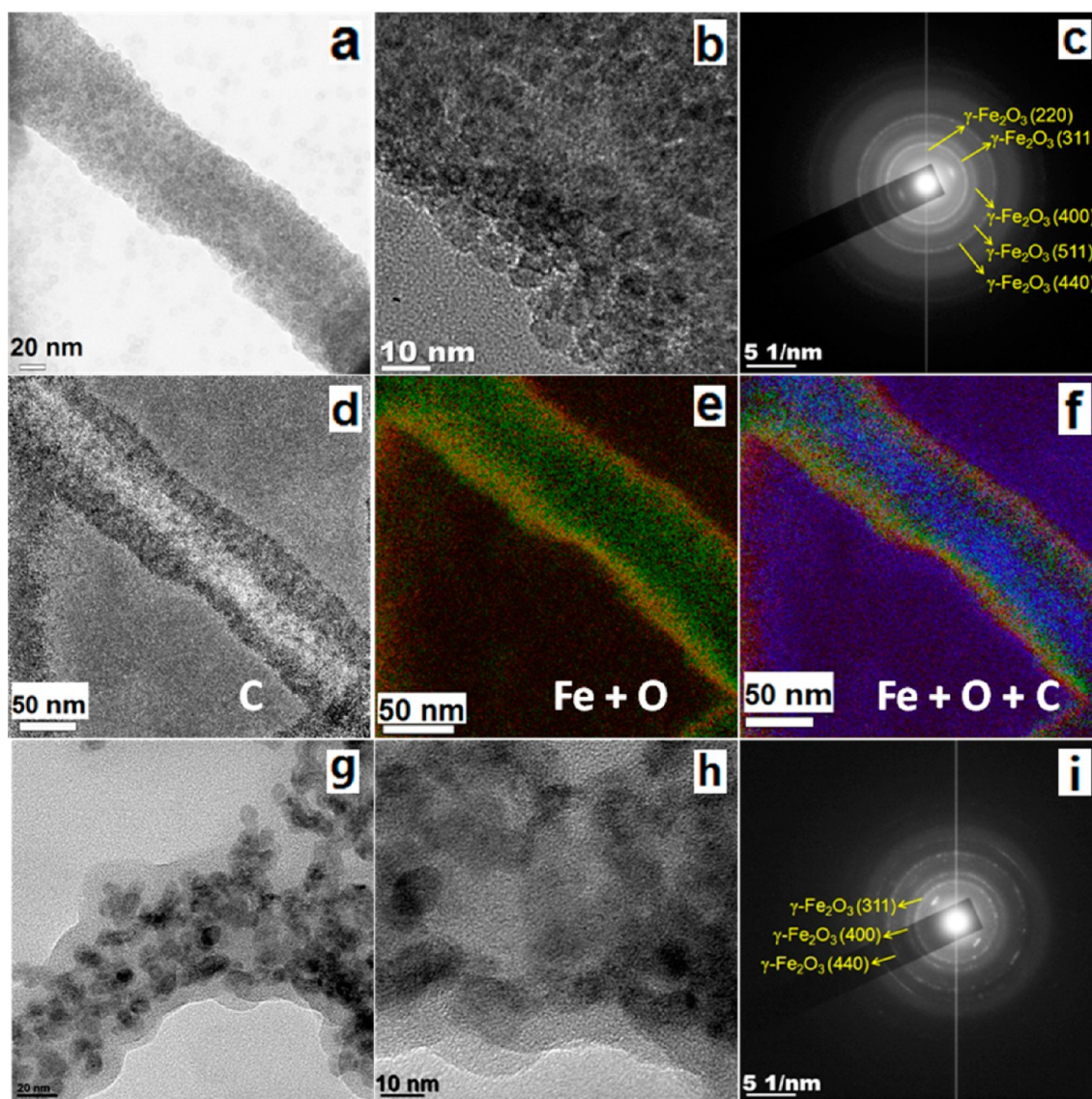
Figure 2. TEM images and SAED of (a, b, c) PP/1.0 MWNTs/5.0% PP-*g*-MA(S)/20.0% Fe MPNCs and their elemental mapping of (d) carbon, (e) Fe (green) + oxygen (red), (f) carbon (blue) + Fe (green) + oxygen (red), and (g, h, i) PP/5.0% PP-*g*-MA(L)/1.0 MWNTs/20.0% Fe MPNCs.

a sample holder, which was located between the rigid beaded airline (APC-7) and the flexible coaxial airline (APC-7) that were connected to the network analyzer. The frequency of electromagnetic waves tested ranged from 100 MHz to 20 GHz. The permeability and permittivity were directly read by the software.

A high-resistance meter (Agilent 4339B) equipped with a resistivity cell (Agilent, 16008B) was used to measure the volume resistivity after inputting the sample thickness. This equipment allows resistivity measurement up to 10^{16} Ω. The source voltage was set at 100 mV and the current was set at 500 μA for all the tested samples. The reported values represented the mean value of five measurements with a deviation less than 10%.

Microscale combustion calorimetry (MCC) was utilized to evaluate the fire hazards by measuring combustion behaviors through using milligram-sized samples.[47,48] To be specific, heat release related parameters including heat release rate (HRR) at different temperatures, peak heat release rate (PHRR), temperature at PHRR (T_{PHRR}), and total heat release (THR) were obtained from MCC. Meanwhile, full width at half-height

(FWHH) was calculated. Here, the data were recorded using a "MCC-2" calorimeter manufactured by Govmark Inc. according to the standard method ASTM D7309-2007 (method A). In a typical measurement, about 3−5 mg of sample was heated from 90 to 600 °C using a heating rate of 1 °C/s in a continuous stream of nitrogen flowing at 80 mL/min. The thermal decomposition products (also called as "fuel gases") were mixed with a 20 mL/min stream of oxygen before entering a 900 °C combustion furnace to complete the nonflaming combustion.

3. RESULTS AND DISCUSSION

3.1. Morphological Characterization. Without any external magnetic field, a self-assembled nanochain consisting of head-to-tail arranged particle building blocks (average particle size 17.7 nm) is observed in the in-situ-synthesized PP/5.0% PP-*g*-MA(S)/20.0% Fe MPNCs (Figure 1a). The high-resolution TEM (HRTEM) image (Figure 1b) shows a core−double shell NPs, i.e., crystalline metallic Fe core (indicated as a 2.03 Å lattice spacing, corresponding to α-Fe

(110) plane, PDF# 06-0696), γ-Fe$_2$O$_3$ inner shell with a 2.09 Å lattice spacing (γ-Fe$_2$O$_3$ (400) plane, PDF# 39-1346), and outer thin layer of graphitized carbon shell with a lattice fringe of 3.50 Å (002). The selected area electron diffraction (SAED) patterns (Figure 1c) further confirm the existence of Fe and γ-Fe$_2$O$_3$ in the formed nanochain as evidenced by the ring patterns corresponding to Fe (110), γ-Fe$_2$O$_3$ (220), (311), (400), (511), and (440). In addition, Fe$_3$C (115), PDF# 00-003-0400, is also observed in the SAED pattern. Therefore, it suggests the coexistence of Fe$_3$C with the core–shell Fe@γ-Fe$_2$O$_3$ NPs in the as-synthesized PP/5.0% PP-g-MA(S)/20.0% Fe MPNCs. When adding only 1.0 wt % MWNTs into the PP matrix in the presence of 5.0% PP-g-MA(S), dispersed nanotubes are observed (Figure 1d).

While adding 1.0 wt % MWNTs to the PP/5.0% PP-g-MA(S)/20.0% Fe MPNCs, γ-Fe$_2$O$_3$ NPs decorated on the MWNTs are observed in the TEM images (Figure 2a,b) and the SAED patterns (Figure 2c, ring patterns corresponding to (220), (311), (400), (511), and (440) planes of γ-Fe$_2$O$_3$, PDF# 39-1346). The average size of the decorated γ-Fe$_2$O$_3$ is about 7.1 nm. In addition, the elemental mappings of carbon, Fe + oxygen, and Fe + oxygen + carbon are demonstrated in Figure 2d,e,f, respectively, confirming the existence of MWNTs coated with Fe$_2$O$_3$ NPs. In addition, when changing the PP-g-MA from "S" to "L", similar morphology of γ-Fe$_2$O$_3$ NPs decorated MWNTs is also observed with an average particle size of 8.3 nm (Figure 2g,h,i).

3.2. XRD Analysis. Wide-angle X-ray diffraction (XRD) patterns were further studied to identify the crystalline structure of the Fe fillers and the PP matrix (Figure 3). In spite of its
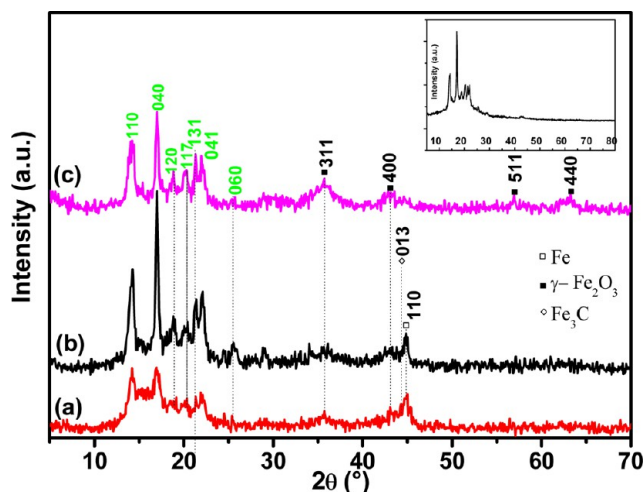
Figure 3. XRD patterns of (a) PP/5.0% PP-g-MA(S)/20.0% Fe, (b) PP/5.0% PP-g-A(S)/1.0 MWNTs/20.0% Fe, and (c) PP/5.0% PP-g-MA(L)/1.0 MWNTs/20.0% Fe MPNCs. Inset: XRD pattern of PP/5.0% PP-g-MA(S)/1.0 MWNTs composites.

simple chemical component, PP with sole hydrocarbons shows remarkable complexity in the crystalline phases. The mainly reported crystalline phases of PP include α- and γ-phases.[49,50] Each phase has its own characteristic peaks and intensity difference in the XRD patterns. Specifically, the intensity of the first peak at 2θ of 14.1° (110) is always stronger than that of the second peak at 2θ of 16.9° (040) for the α-PP; however, this is not true when containing the γ-phase.[49] The γ-phase PP is usually identified from the peak at 2θ of 20.1° (117), while the peak at 2θ of 18.5° (120) is the typical characteristic of α-

phase PP. Previous study has proven that the ratio of γ- to α-phase PP can be determined by the relative peak intensity at 2θ of 20.1° for γ-phase and 2θ of 18.5° for α-phase.[49] Other peaks at 2θ of 21.2°, 21.9°, and 25.4° (Figure 3) correspond to the (131), (041), and (060) crystalline planes of α-phase PP. As shown in Figure 3, all the prepared PP MPNCs are demonstrated with a stronger second peak (040) than the first one (110) except the PP/5.0% PP-g-MA(S)/20.0% Fe MPNCs without MWNTs, indicating less γ phase PP in the PP MPNCs without MWNTs. Moreover, compared with the higher peak intensity of (117) than that of (120) for the pure PP matrix, the relatively less intensive peak at 20.1° (117) than that of the peak at 18.5° (120) after incorporating either the Fe NPs or the MWNTs suggests a reduced amount of γ-phase during the crystallization process.

Earlier studies suggest that PP is inclined to crystallize to γ-phase at a lower cooling rate.[49] Here, the in-situ-formed Fe NPs or the MWNTs decorated with Fe NPs in the PP matrix create a pathway for better heat transfer, and thus the cooling rate is much faster for the MPNCs as compared to that of pure PP. This eventually favors the better energy dissipation when the MPNCs are used for absorbing EM energy.

For the in-situ-synthesized NPs in the PP MPNCs without MWNTs, the XRD pattern (Figure 3a) shows the diffraction peaks at 2θ of 35.6° and 43.2°, corresponding to (311) and (400) crystalline planes of γ-Fe$_2$O$_3$ (PDF# 39-1346). In addition, metallic Fe (110) plane (2θ of 44.7°, PDF# 06-0696) and Fe$_3$C (013) plane (2θ of 44.3°, PDF#00-003-0411) are also observed. This agrees well with the observed core–shell Fe@γ-Fe$_2$O$_3$ NPs in TEM images (Figure 1b). For the PP/5.0% PP-g-MA(S)/1.0 MWNTs, due to the lack of magnetic components, only characteristic XRD peaks of PP matrix are observed (inset of Figure 3). For the PP/5.0% PP-g-MA(S)/20.0% Fe/1.0 wt % MWNTs MPNCs, similar peaks to those of the PP/5.0% PP-g-MA(S)/20.0% Fe were also observed (Figure 3b), indicating the existence of core–shell Fe@γ-Fe$_2$O$_3$ NPs as well as Fe$_3$C after adding MWNTs in the PP/PP-g-MA/Fe MPNCs. When changing the PP-g-MA from "S" to "L", only the characteristic peaks of γ-Fe$_2$O$_3$ [including (311), (400), (511), and (440) planes] are observed (Figure 3c), suggesting the oxidization of Fe NPs in the PP matrix.

3.3. Mössbauer Spectra Analysis. Room temperature ^{57}Fe Mössbauer spectra were investigated to further confirm the chemical environments of the as-obtained NPs and to determine the composition of these NPs. The spectra curves are shown in Figure 4, and the detailed data are listed in Table 1. For the MPNCs filled with only magnetic NPs in the presence of PP-g-MA ("S"), four components are observed after the curve fitting (Figure 4a). The main component is metallic Fe (44%) as evidenced by isomer shift (IS) of 0 mm/s and the corresponding hyperfine field (HI) of 329 kOe (29%)[50,51] and IS of 0.05 mm/s with the corresponding HI of 320 kOe (15%). The second component (23%) is located at a IS of 0.38 mm/s and quadrupole splitting (QS) of 1.20 mm/s (Figure 4a), indicating the Fe^{3+} in a distorted octahedral oxygen environment. 32% cementite is also identified as the third component with IS of 0.2 mm/s and its corresponding HI of 205 kOe.[52] The last component (1%) located at a IS of 0.65 mm/s and QS of 1.80 mm/s (Figure 4a) indicates the presence of Fe$^{2.5+}$ in a distorted octahedral oxygen environment.[53]

For the MPNCs filled with magnetic NPs decorated MWNTs in the presence of PP-g-MA (S), three Fe chemical environments are observed (Figure 4b). The main iron
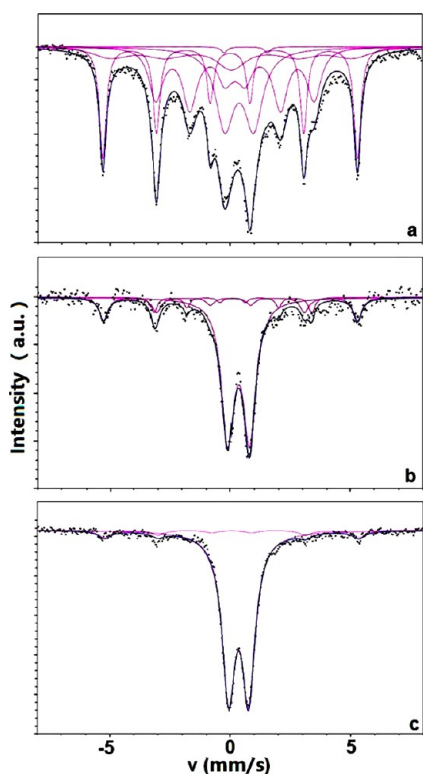
Figure 4. Mössbauer spectra of PP MPNCs with (a) 5.0% PP-*g*-MA(S)/20.0% Fe, (b) 5.0% PP-*g*-A(S)/1.0 MWNTs/20.0% Fe, and (c) PP/5.0% PP-*g*-MA(L)/1.0 MWNTs/20.0% Fe.

Table 1. Room Temperature Mössbauer Spectral Data of the Measured Samples

sample code	composition (%)			
	Fe	Fe³⁺	Fe²·⁵⁺	Fe₃C
a	44	23	1	32
b	18	74		8
c	8	92		

[a]PP/5.0% PP-*g*-MA(S)/20.0% Fe. [b]PP/5.0% PP-*g*-A(S)/1.0 MWNTs/20.0% Fe. [c]PP/5.0% PP-*g*-MA(L)/1.0 MWNTs/20.0% Fe MPNCs.

component in the MPNCs is changed from metallic Fe to oxide (Fe^{3+}, 74%) after adding 1.0 wt % MWNTs, which is evidenced by Fe^{3+} in the distorted octahedral oxygen environment (IS of 0.35 mm/s and QS of 0.90 mm/s).[54,55] The second rich species of Fe here is metallic Fe (18%, IS of 0 mm/s with the corresponding HI of 329 kOe). The last component is 8% cementite (IS of 0.10 mm/s and HI of 202 kOe). It can thus be concluded that further oxidation took place when adding 1.0 MWNTs into the PP/5.0 wt % PP-*g*-MA (S)/20.0 wt % Fe MPNCs.

Different Fe chemical environments are observed when changing the PP-*g*-MA. Here, for PP/1.0 wt % MWNTs/5.0 wt % PP-*g*-MA ("L")/20.0 wt % Fe MPNCs, two components are observed after the curve fitting (Figure 4c). The main component is 92% Fe^{3+} in the distorted octahedral oxygen environment (IS of 0.35 mm/s and QS of 0.83 mm/s). The second species is metallic Fe (8%, IS of 0.06 mm/s with the corresponding HI of 327 kOe). Hence, the molecular weight of PP-*g*-MA plays an important role on the oxidation of Fe NPs in the synthesized MPNCs.

Under constant heating in the PP/PP-*g*-MA/xylene solution, $Fe(CO)_5$ underwent a series of thermal decomposition reactions and formed metallic Fe NPs upon releasing carbon monoxide.[50,51,56] Oxidization took place on the surface of Fe NPs, and iron oxides were formed during the open air synthesis condition. In our previous work, PP-*g*-MA was found to be chemically bound onto the oxide shell of these in-situ-formed core–shell NPs.[57] Moreover, the high concentration chemical bonding of PP-*g*-MA on the surface of these magnetic NPs can prevent further oxidization of the core–shell NPs.[57] Here, the short chain PP-*g*-MA (S) has more MA groups than its long chain counterpart (L), which are believed to be responsible for the stronger stability of thus formed $Fe@\gamma\text{-}Fe_2O_3$ NPs against further oxidation.[58] However, for the PP-*g*-MA (L), it is not effective enough to passivate the shell against further oxidization of the magnetic Fe core. Therefore, more metallic Fe components are observed in the PP MPNCs with PP-*g*-MA (S) as evidenced by the Mössbauer spectra analysis.

3.4. Magnetic Property. Room temperature magnetic property reveals that the PP/5.0 wt % PP-*g*-MA (S)/20.0 wt % Fe MPNCs exhibit a saturation magnetization (M_s) of 20.5 emu/g-composites (Figure 5). In addition, a clear magnetic
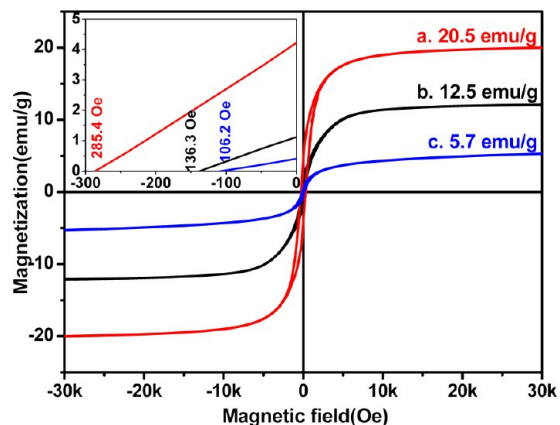
Figure 5. Magnetic hysteresis of (a) PP/5.0% PP-*g*-MA(S)/20.0% Fe, (b) PP/5.0% PP-*g*-A(S)/1.0 MWNTs/20.0% Fe, and (c) PP/5.0% PP-*g*-MA(L)/1.0 MWNTs/20.0% Fe MPNCs.

hysteresis loop with a large coercivity (H_c) of 285.4 Oe (inset of Figure 5) is observed, indicating a hard ferromagnetic behavior (material with H_c greater than 200 Oe is defined as hard ferromagnetic, and soft ferromagnetic has H_c smaller than 200 Oe).[57,59] Nonetheless, both decreased M_s (from 20.5 to 12.5 emu/g) and H_c (from 285.4 to 136.3 Oe) are observed when adding 1.0 wt % MWNTs into the PP/5.0 wt % PP-*g*-MA (S)/20.0 wt % Fe MPNCs. For the PP/1.0 wt % MWNTs/20.0 wt % Fe MPNCs in the presence of 5.0 wt % PP-*g*-MA (L), even lower M_s of 5.7 emu/g-composites with H_c of 106.2 Oe is observed (Figure 5). As for the difference in H_c, magnetically hard behavior becomes magnetically soft after adding MWNTs into the MPNCs even though the fact that higher H_c should be obtained from higher anisotropic effect of the $Fe@Fe_2O_3$ NPs decorated on MWNTs.

It is clear that the parameters to cause the difference in magnetic properties for all the as-obtained PP MPNCs are mainly attributed to the two aspects, i.e., the addition of MWNTs and the variation in the molecular weight of PP-*g*-MA. Without adding MWNTs, the Fe NPs in the PP matrix are very well passivated by the PP-*g*-MA (S) due to the strong chemical
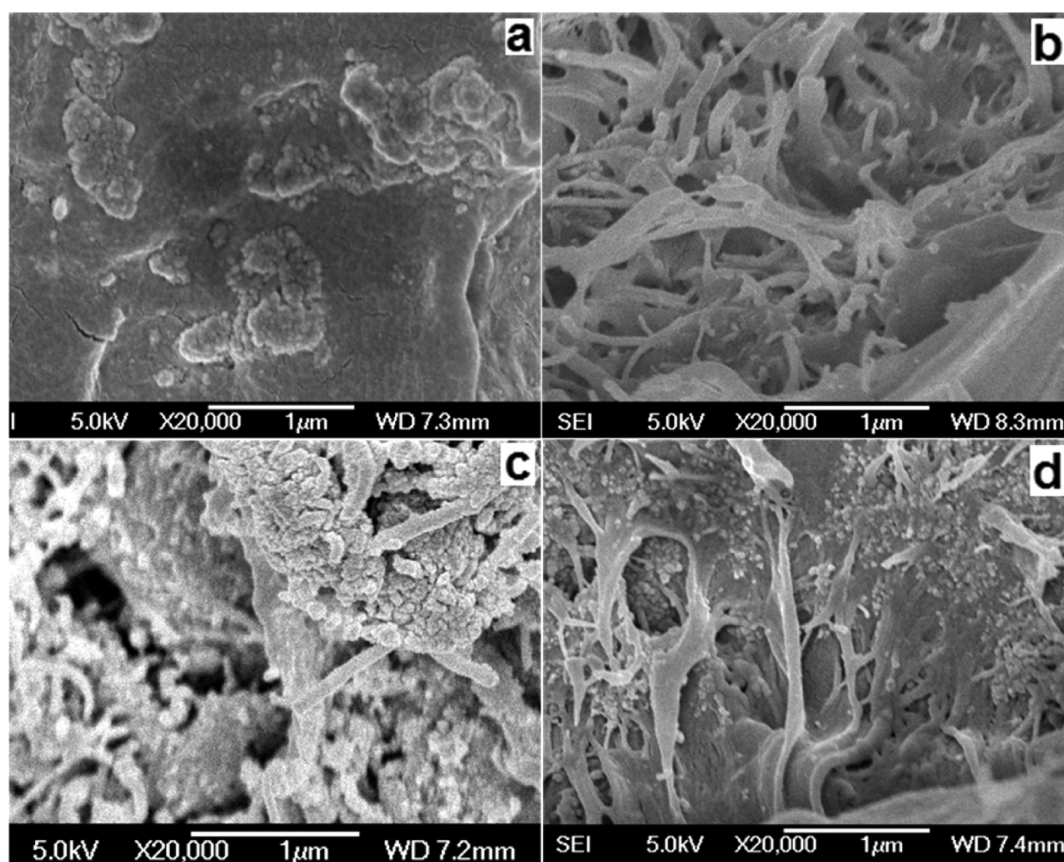
Figure 6. SEM images of (a) PP/5.0% PP-*g*-MA(S)/20.0% Fe, (b) PP/5.0% PP-*g*-MA(S)/1.0 MWNTs, (c) PP/5.0% PP-*g*-A(S)/1.0 MWNTs/ 20.0% Fe, and (d) PP/5.0% PP-*g*-MA(L)/1.0 MWNTs/20.0% Fe MPNCs.

bonding of the MA groups on the surface of Fe NPs as proven in our previous works.[50] As a result, 44% of the metallic Fe remains in the PP matrix, leaving a core−shell Fe @Fe$_2$O$_3$ NPs in the tightly wrapped PP matrix as shown in the TEM images (Figure 1b) and SEM images (Figure 6a). However, compared with the small sized Fe NPs, the addition of bigger MWNTs introduced more free volume in the PP matrix as evidenced by the SEM images in Figure 6b−d.[60] Therefore, more air can penetrate into the PP matrix and contact the surface of the in-situ-formed Fe NPs, leading to further oxidization of metallic Fe core. This explains well with the decreased metallic Fe percentage and the corresponding lower M_s after adding the MWNTs into the PP/5.0 wt % PP-*g*-MA (S)/20.0 wt % Fe MPNCs. When further varying the molecular weight of PP-*g*-MA in the PP MPNCs filled with both MWNTs and Fe NPs, the oxidization of Fe NPs becomes more severe when higher molecular weight PP-*g*-MA (from type S, M_n = 800 to type L, M_n = 8000) is used. This is probably due to the fact that fewer MA functional groups are bounded onto the Fe NPs, leaving more possibility for air to attack the Fe NPs for oxidization.[59]

3.5. Microwave Absorption. Figure 7 shows the frequency-dependent real part (ε') and imaginary part (ε'') of the relative complex permittivity ($\varepsilon_r = \varepsilon' + i\varepsilon''$) and the real part ($\mu'$) and imaginary part ($\mu''$) of the relative complex permeability ($\mu_r = \mu' + i\mu''$) for the as-obtained PP MPNCs. As observed in Figure 7a, for the PP/5.0 wt % PP-*g*-MA(S)/20.0 wt % Fe MPNCs, the ε', μ', and μ'' values all experience a slight decrease (ε' from 6.0 to 4.5, μ' from 1.7 to 1.2, and μ'' from 0.5 to −0.02), while ε'' has demonstrated a slight increase (from 0.5 to 2.0) within the frequency ranging from 100 MHz to 20

GHz. When incorporating 1.0 wt % MWNTs into the PP matrix in the presence of 5.0 wt % PP-*g*-MA (S), the ε and μ curves exhibit different patterns. Both ε' and ε'' are decreased (ε' from 4.7 to 2.8, ε'' from 1.3 to 0.3) within the frequency range from 100 MHz to 20 GHz, while μ' is maintained as 1 and μ'' is maintained as 0 since there is no magnetic components in the PP/1.0 wt % MWNTs composites (Figure 7b). In addition, one peak at 16.8 GHz is observed in both the ε' and ε'' curves. When incorporating 1.0 wt % MWNTs into the PP/5.0 wt % PP-*g*-MA (S)/20.0 wt % Fe MPNCs, both the ε and μ curves exhibit similar trends to those of the PP/5.0 wt % PP-*g*-MA (S)/20.0 wt % Fe MPNCs. In addition, both ε' and ε'' are decreased (ε' from 4.4 to 4.2, ε'' from 0.1 to 0.3), while μ' and μ'' are increased slightly (μ' from 2.1 to 1.2 and μ'' from 0.9 to 0.2) within the frequency range from 100 MHz to 20 GHz (Figure 7c). For the PP/5.0 wt % PP-*g*-MA (L)/1.0 wt % MWNTs/20.0 wt % Fe MPNCs, the ε and μ also show slight difference (ε' from 4.7 to 3.7, ε'' from 0.4 to 0.2, μ' from 1.9 to 1.0, and μ'' from 0.8 to 0.1) within the frequency range from 100 MHz to 20 GHz (Figure 7d). As confirmed from TEM, XRD, and Mössbauer spectra, the variation in the Fe composition on the MWNTs in each of the aforementioned four MPNCs is responsible for the difference in the relative permittivity and permeability.

To further determine the EM wave absorption quantitatively, the RL is calculated based on transmission line theory.[61] The RL of the EM radiation under normal wave incidence at a single layer material surface backed by a perfect conductor can be defined as[62]
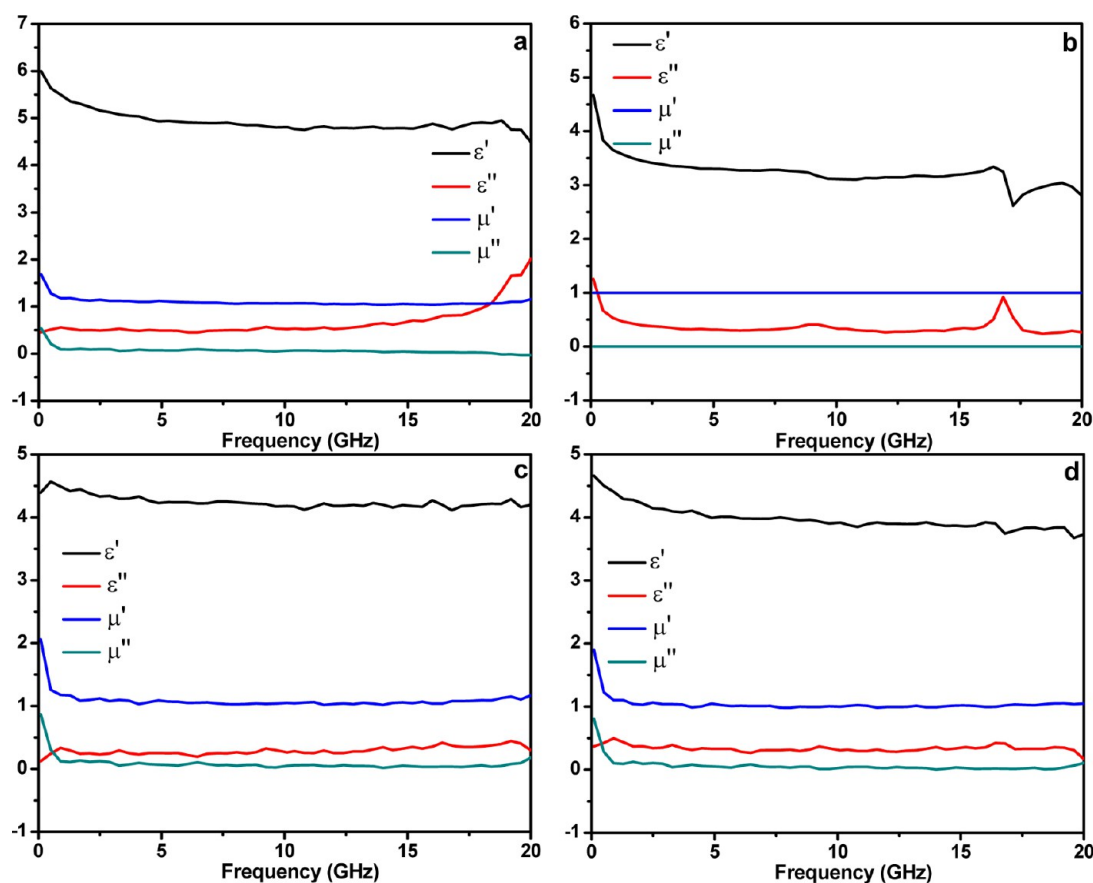
Figure 7. Permittivity and permeability of (a) PP/5.0% PP-*g*-MA(S)/20.0% Fe, (b) PP/5.0% PP-*g*-MA(S)/1.0 MWNTs, (c) PP/5.0% PP-*g*-A(S)/1.0 MWNTs/20.0% Fe, and (d) PP/5.0% PP-*g*-MA(L)/1.0 MWNTs/20.0% Fe MPNCs.

$$\text{RL} = -20 \log \frac{|z_{\text{in}} - 1|}{|z_{\text{in}} + 1|} \tag{1}$$

$$Z_{\text{in}} = \sqrt{\frac{\mu}{\varepsilon}} \tanh\left(-i\frac{2\pi f d}{c}\sqrt{\mu\varepsilon}\right) \tag{2}$$

where Z_{in}, μ, ε, f, d, and c represent the input impedance at the interface of free space and tested specimens, complex permeability, complex permittivity, frequency of EM wave, thickness of the specimen, and the velocity of EM waves in free space, respectively.[16]

The RL of the PP/5.0 wt % PP-*g*-MA (S)/20.0 wt % Fe MPNCs with the sample thickness varied from 3.0 to 7.5 mm was calculated (Figure 8a). The minimum RL reaches −31.5 dB at 18.0 GHz at a thickness of 5.5 mm. Moreover, the bandwidth with the RL below −10 dB is up to 3.1 GHz (from 16.9 to 20.0 GHz), while the bandwidth with the RL below −20 dB is up to 0.8 GHz (from 17.7 to 18.5 GHz). When calculated with a sample thickness of 7.5 mm, the minimum RL reaches −22.3 dB at 13.6 GHz, and the bandwidth with the RL below −10 dB is up to 2.2 GHz (from 12.3 to 14.5 GHz), while the bandwidth with the RL below −20 dB is up to 0.6 GHz (from 13.1 to 13.7 GHz). The RL of the PP/5.0 wt % PP-*g*-MA (S)/1.0 wt % MWNTs MPNCs with the sample thickness varied from 3.0 to 7.5 mm was calculated (Figure 8b). The minimum RL reaches −27.2 dB at 16.8 GHz at a thickness of 7.5 mm. Moreover, the bandwidth with the RL below −10 dB is 1.0 GHz (from 16.2 to 17.2 GHz), while the bandwidth with the RL below −20 dB is 0.2 GHz (from 16.7 to 16.9 GHz). The RL of the PP/5.0 wt %

PP-*g*-MA (S)/1.0 wt % MWNTs/20.0 wt % Fe MPNCs with the sample thickness varied from 3.0 to 7.5 mm was also calculated (Figure 8c). The minimum RL reaches −16.7 dB at 19.6 GHz at a thickness of 5.5 mm. Moreover, the bandwidth with the RL below −10 dB is up to 1.5 GHz (from 18.5 to 20.0 GHz). When calculated with sample thickness of 5.0 mm, there is no minimum RL, and the lowest RL at the highest testing frequency (20.0 GHz) reaches −24.5 dB. This suggests for potential lower RL beyond 20 GHz, which is unavailable due to the frequency limit of the testing instrument. Similarly, for the PP/5.0 wt % PP-*g*-MA (L)/1.0 wt % MWNTs/20.0 wt % Fe MPNCs, there might be a potential minimum RL beyond 20 GHz even though the lowest RL at thickness of 5.0/5.5/7.5 mm is quite smaller than that of the PP MPNCs without MWNTs (Figure 8d).

For the PP/MWNTs composites, the dielectric loss mainly attributes to the relaxation process (may include interfacial polarization, electronic dipole polarization, and orientational polarization) and is the mechanism of the EM absorption.[63] However, as for the PP MPNCs with magnetic NPs decorated MWNTs, the MWNTs may play a negative role on the microwave absorption behaviors of the PP MPNCs within the tested frequency range. The probable reasons for the resulted smaller RL value by introducing MWNTs to form the PP/MWNTs/Fe MPNCs include (1) the decreased M_s resulting from the addition of MWNTs into the PP MPNCs, (2) the eddy current effect, (3) conductivity difference, and (4) geometrical effect of the EM absorbing nanofillers. Low M_s will decrease the magnetic permeability, while eddy current loss
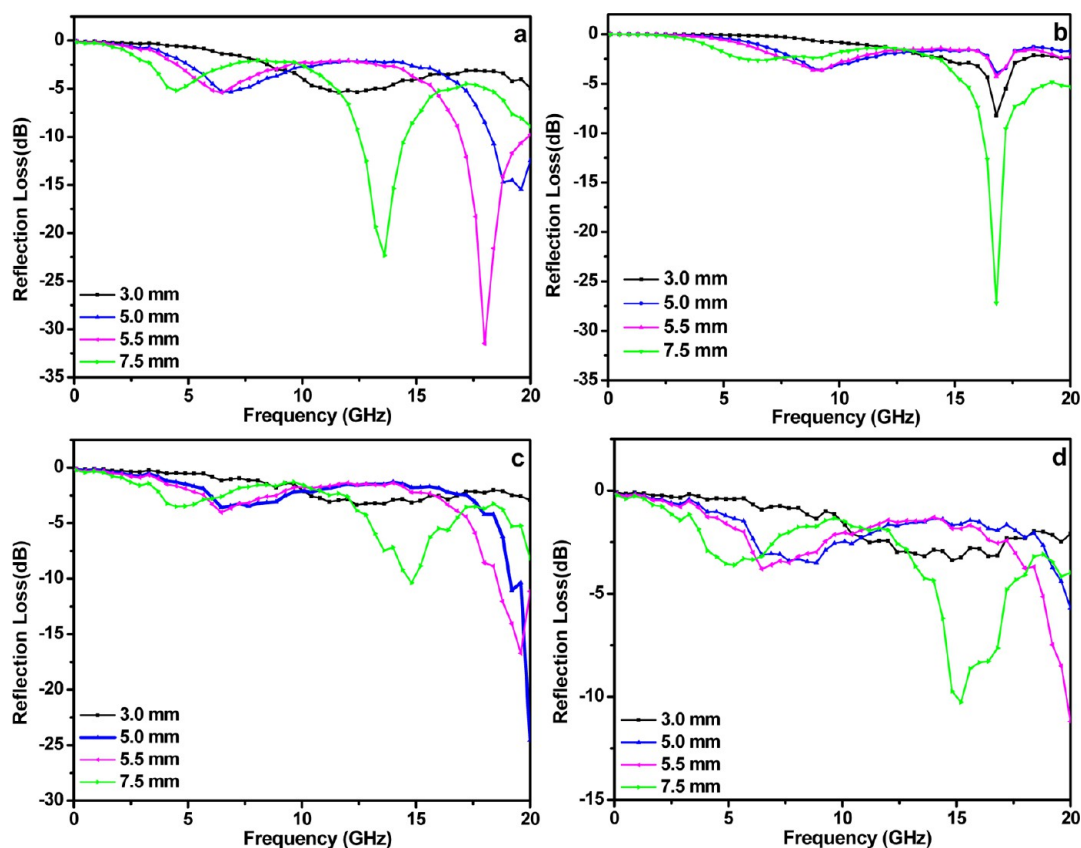
Figure 8. Reflection losses of (a) PP/5.0% PP-*g*-MA(S)/20.0% Fe, (b) PP/5.0% PP-*g*-MA(S)/1.0 MWNTs, (c) PP/5.0% PP-*g*-A(S)/1.0 MWNTs/ 20.0% Fe, and (d) PP/5.0% PP-*g*-MA(L)/1.0 MWNTs/20.0% Fe MPNCs.

effect deteriorates the permeability within the high frequency range. High conductivity will certainly prefer the EM wave reflection, while the geometrical effect like aligned nanostructures will favor the strong EM wave absorption.

For the EM wave absorption applications, the high initial permeability (μ_i) of an EM wave absorber is favorable, and the permeability of ferromagnetic materials can be expressed as eq 3:[64,65]

$$\mu_i = \frac{M_s^2}{akH_cM_s + b\lambda\xi}$$ (3)

where a and b are two constants determined by the material composition, λ is the magnetostriction constant, and ξ is an elastic strain parameter of the crystal.[64] Meanwhile, K is a constant to decide the direction of easy axis, which can be expressed as[64]

$$K = kH_cM_s$$ (4)

It is obvious from the above equations that higher M_s is favorable to the increase of μ_i, which in turn enhances the EM wave absorption. Therefore, among all the as-prepared MPNCs, the highest M_s of the PP MPNCs without MWNTs should give the highest RL, which can be confirmed in Figure 8.

For the ferromagnetic absorber, the EM absorption properties are usually subjected to degradation caused by the eddy current effect in the high frequency region. The eddy current loss can be evaluated by eq 5:[16]

$$\mu'' \approx 2\pi\mu_0(\mu')^2\sigma d^2 f/3$$ (5)

where μ'' is the imaginary permeability and μ' is the real permeability of the absorber, σ (S m^{-1}) is the electrical conductivity, μ_0 (H m^{-1}) is the permeability in a vacuum, d is the thickness of the absorber, and f is the frequency. If the RL is attributed from the eddy current loss effect, the value of C_0 [$C_0 = \mu''(\mu')^{-2}f^{-1}$] is independent of the variation of the testing frequency. As shown in inset of Figure 9, the C_0 as a function of frequency curves clearly indicates that the PP/5.0 wt % PP-*g*-MA (S)/20.0 wt % Fe MPNCs with MWNTs have a significant eddy current effect as evidenced by the almost constant C_0 values within the frequency range from 5.0 to 20.0 GHz. In addition, a reduced eddy current effect is observed in the
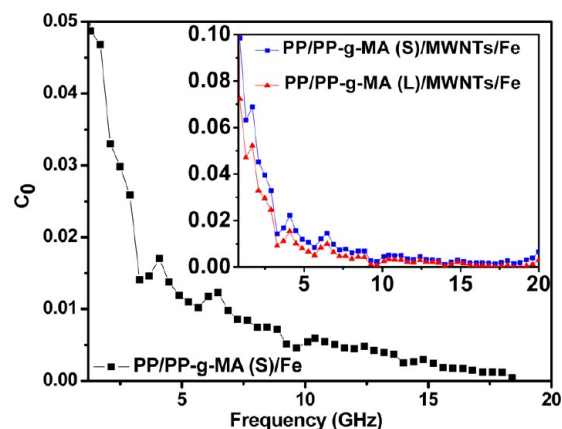
Figure 9. C_0 curves as a function of frequency for the PP MPNCs.

MPNCs without MWNTs, which is confirmed by the frequency-dependent C_0 values (Figure 9).

Figure 10 further demonstrates the volume resistivity (R_v) of the as-prepared PP MPNCs. The PP/20.0 wt % Fe/5.0 wt %
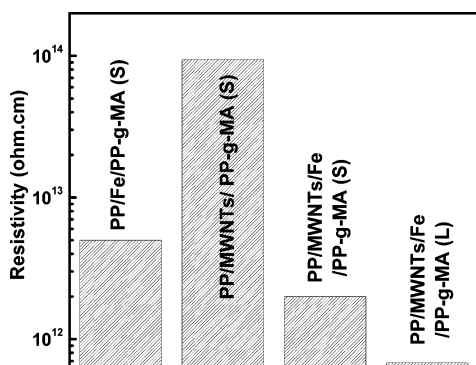
Figure 10. Resistivity of all the as-obtained PP MPNCs.

PP-g-MA (S) MPNCs exhibit a R_v of ~5 × 10^{12} ohm·cm (Ω·cm), while the PP/5.0 wt % PP-g-MA (S)/1.0 wt % MWNTs composites have a R_v of 9.4 × 10^{13} Ω·cm. In addition, R_v is decreased to ~2 × 10^{12} Ω·cm for the PP/1.0 wt % MWNTs/ 20.0 wt % Fe/5.0 wt % PP-g-MA(S) MPNCs. When further changing the PP-g-MA from "S" to "L", a similar R_v of 6.8 × 10^{11} Ω·cm is observed. This suggests that with 1.0 wt % MWNTs, 20.0 wt % Fe@Fe$_2$O$_3$ NPs, and 1.0 wt % MWNTs decorated with 20.0 wt % Fe@Fe$_2$O$_3$ NPs/Fe$_2$O$_3$ NPs, the obtained PP nanocomposites remain insulated, probably due to the tightly covered nonconductive PP-g-MA on the surface of these nanofillers to prevent the direct contact among the NPs. Usually, the EM wave absorption efficiency of the polymer-based composites depends on many factors, including the electrical conductivity, dielectric constant, and magnetic permeability.[21] Also, ideal performance of one EM wave absorbing material (consisted of both magnetic and dielectric components) is mainly attributed to two factors: impedance matching and EM wave attenuation. The ideal condition for a perfect absorber is that the conductive component decorated with relatively insulating magnetic component can lower the permittivity of the absorber and improve the equality between permittivity and permeability to facilitate the balance of impedance matching.[34,35] While the permittivity is correlated to the conductivity (resistivity),[21,66] the impedance match is the reason that better EM wave absorption of the PP/Fe MPNCs than the PP/MWNTs/Fe MPNCs. The lower R_v observed for the PP MPNCs without MWNTs can provide better impedance match between magnetic loss and the dielectric loss. This also explains why the presence of MWNTs in the PP/MWNTs/Fe MPNCs triggered the observed eddy current loss effect.

For the EM wave absorption, apart from the dielectric loss and magnetic loss, the EM wave may also be absorbed due to the geometrical effect, as found in the Ni nanowires[67] and MWNTs composites.[68] When the thickness (d) of absorber satisfies the equation $d = n\lambda_m/4$ ($n = 1, 3, 5, ...$), where λ_m is the wavelength in the absorber at some specific frequency, the incident and reflected waves in the absorber are out of phase 180° and thus the reflected waves at the free space−absorber interface are totally canceled.[69] Here, the alignment of magnetic NPs into well-defined rod- and chain- like structures is believed to increase the geometrical effect when an EM wave radiated

onto these materials, leading to the improved EM wave absorption. The head-to-tail arrangement of Fe@Fe$_2$O$_3$ core−shell NPs in the PP matrix without MWNTs may also have this geometrical effect. Compared with the reported paraffin wax composites incorporated with 25.0 wt % graphene@Fe$_3$O$_4$ (maximum RL of 11.7 dB at a sample thickness of 2.0 mm and EM absorption frequency bandwidth at RL values under the 10 dB is 1.1 GHz) and graphene@Fe$_3$O$_4$@SiO$_2$ hierarchical nanofillers (the maximum RL of 22.1 dB and the frequency bandwidth at RL values under 10 dB is 2.2 GHz),[70] our in-situ one-pot formed PP MPNCs exhibit better EM wave absorption performance with lower filler loading. Meanwhile, even compared with the carbon nanotubes encapsulated with metallic iron filled epoxy composites (16.7% filler loading),[71] the as-prepared PP MPNCs also demonstrate the advantages such as easiness of composites fabrication and lower RL.

3.6. Combustion Behavior and Fire Hazard. MCC was utilized to further evaluate the fire hazards[72,73] of pure PP and its MPNCs. Figure 11 depicts the HRR vs temperature curves,
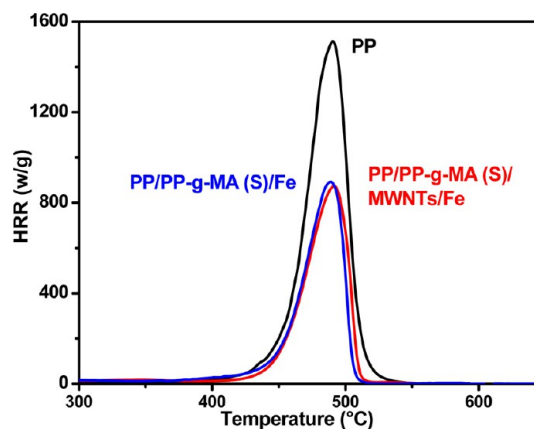
Figure 11. HRR as a function of temperature for pure PP and the PP MPNCs.

Table 2. MCC Data of the Measured Samples

composition	PHRR (w/g)	PHRR reduction (%)	T_{PHRR} (°C)	THR (kJ/g)	FWHH (s)
PP	1513.0		490.4	40.6	24.2
a	890.6	41.1	488.8	33.1	31.2
b	872.3	42.3	491.8	33.4	33.4
c	867.2	42.6	489.8	30.8	31.3

[a]PP/5.0% PP-g-MA(S)/20.0% Fe. [b]PP/5.0% PP-g-A(S)/1.0 MWNTs/20.0% Fe. [c]PP/5.0% PP-g-MA(L)/1.0 MWNTs/20.0% Fe MPNCs.

and Table 2 lists the corresponding heat release parameters. HRR is the single most important parameter to assess the fire hazard of one flammable material.[74] The higher PHRR one material generates under a specific heat flux, the more dangerous it will become under a fire accident. Pure PP is a highly flammable material with an observed PHRR of 1513.0 w/g and THR of 40.6 kJ/g. Meanwhile, the initial thermal decomposition and T_{PHRR} are ~400 and 490.4 °C, respectively.

For the PP/5.0 wt % PP-g-MA/20.0 wt % Fe MPNCs, the PHRR is decreased from 1513.0 to 872.3 W/g (~42.3% reduction), THR is decreased from 40.6 to 33.4 W/g, and the

initial decomposition temperature is increased from 490.4 to 491.8 °C upon adding the Fe NPs (Table 2). Apparently, with excluding the dilution of combustible PP through the 20.0 wt % non-hydrocarbon nanofillers, an additional 22.3% decrease in PHRR indicates a flame retardancy effect of these in-situ-formed Fe NPs on the PP matrix. More precisely, a barrier effect from these Fe NPs was believed to be responsible for this flame retardancy as suggested by the delayed initial decomposition temperature. During the thermal decomposition, heat and mass transfers between gas and condense phases were slowed down by forming an insulating layer from the in-situ-formed Fe NPs when the MPNCs were exposed under heat, and thus fast decomposition of polymeric PP matrix was suppressed.[75] In addition, the FWHH of the PP/5.0 wt % PP-g-MA/20.0 wt % Fe MPNCs is increased to 33.4 compared with that of 24.2 s for pure PP, further suggesting a flame-retardant mechanism with longer heat release duration.[60] No significant PHRR reduction is observed when either adding 1.0 wt % MWNTs or varying the molecular weight of PP-g-MA in the PP/Fe MPNCs (Table 2). Unlike the catalytic effect of cobalt−cobalt oxide core−shell NPs and PP-g-MA on reducing the fire hazards of PP,[47] the as-prepared Fe@Fe$_2$O$_3$ core−shell NPs here did not show any catalytic effect on PP. Nonetheless, these in-situ-formed NPs in the PP matrix obviously have demonstrated the advantage by shielding the polymeric matrix from fast thermal degradation at high temperatures.

4. CONCLUSION

An in-situ one-pot method is developed to prepare the PP MPNCs reinforced with either Fe@Fe$_2$O$_3$ core−shell NPs or MWNTs decorated with Fe@Fe$_2$O$_3$ core−shell NPs in the presence of surfactant PP-g-MA, which is promising for high efficiency EM wave absorption application with controllable frequency range at GHz. Moreover, the significantly reduced flammability of these MPNCs (compared with pure PP) is good for making safer EM wave absorber to satisfy stringent industrial and federal standards. The PP MPNCs without MWNTs clearly have demonstrated promising EM wave absorption without suffering from eddy current loss effect. A minimum −31.5 dB RL corresponding to more than 99.9% EM wave can be reached and different reflection loss frequency range can be achieved by simply varying the absorber thickness. It is also interesting to discover that the addition of small amount of MWNTs (i.e., 1.0 wt %) during the fabrication of PP/Fe MPNCs plays a negative role on improving the RL due to the reduced magnetization and the eddy current loss effect. Nonetheless, the PP MPNCs with MWNTs show potential for high-frequency EM wave absorption as indicated by its low reflection loss below −20 dB at 20.0 GHz. Therefore, the prevention against the oxidation of the as-prepared iron NPs can favor the further enhancement in the microwave absorption performance, i.e., the RL frequency bandwidth under 10 dB.[76] The preparation of MPNCs with the in-situ-formed hierarchical nanostructure fillers can also be applied to synthesize other fillers such as graphene decorated magnetic nanostructures and other binary components such as iron oxide/barium titanate for high performance lightweight EM wave absorption materials.[77,78]

■ AUTHOR INFORMATION

Corresponding Authors
*E-mail: zhanhu.guo@lamar.edu; phone (409) 880 7654 (Z.G.).
*E-mail: suying.wei@lamar.edu, phone (409) 880 7976 (S.W.).
*E-mail: jrliu@sdu.edu.cn (J.L.).
Notes
The authors declare no competing financial interest.

■ ACKNOWLEDGMENTS

■ REFERENCES

(1) Yan, D.-X.; Ren, P.-G.; Pang, H.; Fu, Q.; Yang, M.-B.; Li, Z.-M. Efficient Electromagnetic Interference Shielding of Lightweight Graphene/Polystyrene Composite. *J. Mater. Chem.* **2012**, *22*, 18772−18774.

(2) Eswaraiah, V.; Sankaranarayanan, V.; Ramaprabhu, S. Functionalized Graphene−PVDF Foam Composites for Emi Shielding. *Macromol. Mater. Eng.* **2011**, *296*, 894−898.

(3) Group, T. I. S. Brain Tumour Risk in Relation to Mobile Telephone Use: Results of the Interphone International Case-Control Study. *Int. J. Epidemiol.* **2010**, *39*, 675−694.

(4) Hansteen, I.-l.; LaGeide, L.; Clausen, K. O.; Haugan, V.; Svendsen, M.; Eriksen, J. G.; Skiaker, R.; Hauger, E.; Vistnes, A. I.; Kure, E. H. Cytogenetic Effects of 18.0 and 16.5 GHz Microwave Radiation on Human Lymphocytes in Vitro. *Anticancer Res.* **2009**, *29*, 2885−2892.

(5) Liu, J.; Cheng, J.; Che, R.; Xu, J.; Liu, M.; Liu, Z. Synthesis and Microwave Absorption Properties of Yolk−Shell Microspheres with Magnetic Iron Oxide Cores and Hierarchical Copper Silicate Shells. *ACS Appl. Mater. Interfaces* **2013**, *5*, 2503−2509.

(6) Zhang, X.-J.; Wang, G.-S.; Cao, W.-Q.; Wei, Y.-Z.; Liang, J.-F.; Guo, L.; Cao, M.-S. Enhanced Microwave Absorption Property of Reduced Graphene Oxide (RGO)-MnFe$_2$O$_4$ Nanocomposites and Polyvinylidene Fluoride. *ACS Appl. Mater. Interfaces* **2014**, *6*, 7471−7478.

(7) Chaubey, G. S.; Barcena, C.; Poudyal, N.; Rong, C.; Gao, J.; Sun, S.; Liu, J. P. Synthesis and Stabilization of FeCo Nanoparticles. *J. Am. Chem. Soc.* **2007**, *129*, 7214−7215.

(8) Rahman, F.; Langford, K. H.; Scrimshaw, M. D.; Lester, J. N. Polybrominated Diphenyl Ether (PBDE) Flame Retardants. *Sci. Total Environ.* **2001**, *275*, 1−17.

(9) Leslie-Pelecky, D. L.; Rieke, R. D. Magnetic Properties of Nanostructured Materials. *Chem. Mater.* **1996**, *8*, 1770−1783.

(10) Tartaj, P.; Morales, M. P.; Veintemillas-Verdaguer, S.; González-Carreno, T.; Serna, C. J. The Preparation of Magnetic Nanoparticles for Applications in Biomedicine. *J. Phys. D: Appl. Phys.* **2003**, *36*, R182.

(11) Crooks, R. M.; Zhao, M.; Sun, L.; Chechik, V.; Yeung, L. K. Dendrimer-Encapsulated Metal Nanoparticles: Synthesis, Characterization, and Applications to Catalysis. *Acc. Chem. Res.* **2001**, *34*, 181−190.

(12) Zhang, J.; Xu, S.; Kumacheva, E. Polymer Microgels: Reactors for Semiconductor, Metal, and Magnetic Nanoparticles. *J. Am. Chem. Soc.* **2004**, *126*, 7908−7914.

(13) Ferrando, R.; Jellinek, J.; Johnston, R. L. Nanoalloys: From Theory to Applications of Alloy Clusters and Nanoparticles. *Chem. Rev.* **2008**, *108*, 845.

(14) Singh, P.; Babbar, V.; Razdan, A.; Srivastava, S.; Goel, T. Microwave Absorption Studies of Ca−NiTi Hexaferrite Composites in X-Band. *Mater. Sci. Eng., B* **2000**, *78*, 70−74.

(15) Haijun, Z.; Zhichao, L.; Chengliang, M.; Xi, Y.; Liangying, Z.; Mingzhong, W. Complex Permittivity, Permeability, and Microwave Absorption of Zn- and Ti-Substituted Barium Ferrite by Citrate Sol—Gel Process. *Mater. Sci. Eng., B* **2002**, *96*, 289—295.

(16) Zhu, J.; Wei, S.; Haldolaarachchige, N.; Young, D. P.; Guo, Z. Electromagnetic Field Shielding Polyurethane Nanocomposites Reinforced with Core—Shell Fe—Silica Nanoparticles. *J. Phys. Chem. C* **2011**, *115*, 15304—15310.

(17) McConnell, H. M. Eddy-Current Phenomena in Ferromagnetic Materials. *IEEE Trans. Commun.* **1954**, *73*, 226—235.

(18) Yu, Z.; Yao, Z.; Zhang, N.; Wang, Z.; Li, C.; Han, X.; Wu, X.; Jiang, Z. Electric Field-Induced Synthesis of Dendritic Nanostructured A-Fe for Electromagnetic Absorption Application. *J. Mater. Chem. A* **2013**, *1*, 4571—4576.

(19) Thomassin, J.-M.; Pagnoulle, C.; Bednarz, L.; Huynen, I.; Jerome, R.; Detrembleur, C. Foams of Polycaprolactone/MWNT Nanocomposites for Efficient Emi Reduction. *J. Mater. Chem.* **2008**, *18*, 792—796.

(20) Ling, J.; Zhai, W.; Feng, W.; Shen, B.; Zhang, J.; Zheng, W. G. Facile Preparation of Lightweight Microcellular Polyetherimide/Graphene Composite Foams for Electromagnetic Interference Shielding. *ACS Appl. Mater. Interfaces* **2013**, *5*, 2677—2684.

(21) Chen, Z.; Xu, C.; Ma, C.; Ren, W.; Cheng, H. M. Lightweight and Flexible Graphene Foam Composites for High-Performance Electromagnetic Interference Shielding. *Adv. Mater.* **2013**, *25*, 1296—1300.

(22) Maiti, S.; Shrivastava, N. K.; Suin, S.; Khatua, B. B. Polystyrene/MWCNT/Graphite Nanoplate Nanocomposites: Efficient Electromagnetic Interference Shielding Material through Graphite Nanoplate—MWCNT—Graphite Nanoplate Networking. *ACS Appl. Mater. Interfaces* **2013**, *5*, 4712—4724.

(23) Bai, X.; Zhai, Y.; Zhang, Y. Green Approach to Prepare Graphene-Based Composites with High Microwave Absorption Capacity. *J. Phys. Chem. C* **2011**, *115*, 11673—11677.

(24) Zhang, H.-B.; Yan, Q.; Zheng, W.-G.; He, Z.; Yu, Z.-Z. Tough Graphene—Polymer Microcellular Foams for Electromagnetic Interference Shielding. *ACS Appl. Mater. Interfaces* **2011**, *3*, 918—924.

(25) Zhou, J.; He, J.; Li, G.; Wang, T.; Sun, D.; Ding, X.; Zhao, J.; Wu, S. Direct Incorporation of Magnetic Constituents within Ordered Mesoporous Carbon—Silica Nanocomposites for Highly Efficient Electromagnetic Wave Absorbers. *J. Phys. Chem. C* **2010**, *114*, 7611—7617.

(26) Zhou, H.; Wang, J.; Zhuang, J.; Liu, Q. Synthesis and Electromagnetic Interference Shielding Effectiveness of Ordered Mesoporous Carbon Filled Poly(methyl methacrylate) Composite Films. *RSC Adv.* **2013**, *3*, 23715—23721.

(27) Wang, G.-S.; Zhang, X.-J.; Wei, Y.-Z.; He, S.; Guo, L.; Cao, M.-S. Polymer Composites with Enhanced Wave Absorption Properties Based on Modified Graphite and Polyvinylidene Fluoride. *J. Mater. Chem. A* **2013**, *1*, 7031—7036.

(28) Chen, Y.; Li, Y.; Yip, M.; Tai, N. Electromagnetic Interference Shielding Efficiency of Polyaniline Composites Filled with Graphene Decorated with Metallic Nanoparticles. *Compos. Sci. Technol.* **2013**, *80*, 80—86.

(29) Yang, Y.; Gupta, M. C.; Dudley, K. L.; Lawrence, R. W. Novel Carbon Nanotube-Polystyrene Foam Composites for Electromagnetic Interference Shielding. *Nano Lett.* **2005**, *5*, 2131—2134.

(30) Zhang, X.; Alloul, O.; He, Q.; Zhu, J.; Verde, M. J.; Li, Y.; Wei, S.; Guo, Z. Strengthened Magnetic Epoxy Nanocomposites with Protruding Nanoparticles on the Graphene Nanosheets. *Polymer* **2013**, *54*, 3594—3604.

(31) Wang, W.; Gumfekar, S.; Jiao, Q.; Zhao, B. Ferrite-Grafted Polyaniline Nanofibers as Electromagnetic Shielding Materials. *J. Mater. Chem. C* **2013**, *1*, 2851—2859.

(32) Cao, M.-S.; Yang, J.; Song, W.-L.; Zhang, D.-Q.; Wen, B.; Jin, H.-B.; Hou, Z.-L.; Yuan, J. Ferroferric Oxide/Multiwalled Carbon Nanotube vs Polyaniline/Ferroferric Oxide/Multiwalled Carbon Nanotube Multiheterostructures for Highly Effective Microwave Absorption. *ACS Appl. Mater. Interfaces* **2012**, *4*, 6949—6956.

(33) Xu, P.; Han, X.; Jiang, J.; Wang, X.; Li, X.; Wen, A. Synthesis and Characterization of Novel Coralloid Polyaniline/BaFe$_{12}$O$_{19}$ Nanocomposites. *J. Phys. Chem. C* **2007**, *111*, 12603—12608.

(34) Zong, M.; Huang, Y.; Zhao, Y.; Sun, X.; Qu, C.; Luo, D.; Zheng, J. Facile Preparation, High Microwave Absorption and Microwave Absorbing Mechanism of RGO—Fe$_3$O$_4$ Composites. *RSC Adv.* **2013**, *3*, 23638—23648.

(35) Singh, A. P.; Mishra, M.; Sambyal, P.; Gupta, B. K.; Singh, B. P.; Chandra, A.; Dhawan, S. K. Encapsulation of γ-Fe$_2$O$_3$ Decorated Reduced Graphene Oxide in Polyaniline Core—Shell Tubes as an Exceptional Tracker for Electromagnetic Environmental Pollution. *J. Mater. Chem. A* **2014**, *2*, 3581—3593.

(36) Shen, B.; Zhai, W.; Tao, M.; Ling, J.; Zheng, W. Lightweight, Multifunctional Polyetherimide/Graphene@Fe$_3$O$_4$ Composite Foams for Shielding of Electromagnetic Pollution. *ACS Appl. Mater. Interfaces* **2013**, *5*, 11383—11391.

(37) Wang, Q.; O'Hare, D. Recent Advances in the Synthesis and Application of Layered Double Hydroxide (LDH) Nanosheets. *Chem. Rev.* **2012**, *112*, 4124—4155.

(38) Xu, X.-B.; Li, Z.-M.; Dai, K.; Yang, M.-B. Anomalous Attenuation of the Positive Temperature Coefficient of Resistivity in a Carbon-Black-Filled Polymer Composite with Electrically Conductive in Situ Microfibrils. *Appl. Phys. Lett.* **2006**, *89*, 032105—032105—3.

(39) Kong, L.; Yin, X.; Zhang, Y.; Yuan, X.; Li, Q.; Ye, F.; Cheng, L.; Zhang, L. Electromagnetic Wave Absorption Properties of Reduced Graphene Oxide Modified by Maghemite Colloidal Nanoparticle Clusters. *J. Phys. Chem. C* **2013**, *117*, 19701—19711.

(40) Xia, Y.; Xiong, Y.; Lim, B.; Skrabalak, S. E. Shape-Controlled Synthesis of Metal Nanocrystals: Simple Chemistry Meets Complex Physics? *Angew. Chem., Int. Ed.* **2009**, *48*, 60—103.

(41) Dumestre, F.; Chaudret, B.; Amiens, C.; Fromen, M.-C.; Casanove, M.-J.; Renaud, P.; Zurcher, P. Shape Control of Thermodynamically Stable Cobalt Nanorods through Organometallic Chemistry. *Angew. Chem., Int. Ed.* **2002**, *41*, 4286—4289.

(42) Puntes, V. F.; Krishnan, K. M.; Alivisatos, A. P. Colloidal Nanocrystal Shape and Size Control: The Case of Cobalt. *Science* **2001**, *291*, 2115—2117.

(43) He, Q.; Yuan, T.; Yan, X.; Luo, Z.; Haldolaarachchige, N.; Young, D. P.; Wei, S.; Guo, Z. One-Pot Synthesis of Size- and Morphology-Controlled 1-D Iron Oxide Nanochains with Manipulated Magnetic Properties. *Chem. Commun.* **2014**, *50*, 201—203.

(44) Chen, D.; Wang, G.-S.; He, S.; Liu, J.; Guo, L.; Cao, M.-S. Controllable Fabrication of Mono-Dispersed RGO—Hematite Nanocomposites and Their Enhanced Wave Absorption Properties. *J. Mater. Chem. A* **2013**, *1*, 5996—6003.

(45) Zhang, H.; Xie, A.; Wang, C.; Wang, H.; Shen, Y.; Tian, X. Novel RGO/A-Fe$_2$O$_3$ Composite Hydrogel: Synthesis, Characterization and High Performance of Electromagnetic Wave Absorption. *J. Mater. Chem. A* **2013**, *1*, 8547—8552.

(46) Lei, C.; Chen, D.; Wu, B.; Xu, Y.; Li, S.; Huang, W. Melt-Grafting Mechanism Study of Maleic Anhydride onto Polypropylene with 1-Decene as the Second Monomer. *J. Appl. Polym. Sci.* **2011**, *121*, 3724—3732.

(47) He, Q.; Yuan, T.; Wei, S.; Guo, Z. Catalytic and Synergistic Effects on Thermal Stability and Combustion Behavior of Polypropylene: Influence of Maleic Anhydride Grafted Polypropylene Stabilized Cobalt Nanoparticles. *J. Mater. Chem. A* **2013**, *1*, 13064—13075.

(48) Yang, C. Q.; He, Q.; Lyon, R. E.; Hu, Y. Investigation of the Flammability of Different Textile Fabrics Using Micro-Scale Combustion Calorimetry. *Polym. Degrad. Stab.* **2010**, *95*, 108—115.

(49) Zhu, J.; Wei, S.; Li, Y.; Sun, L.; Haldolaarachchige, N.; Young, D. P.; Southworth, C.; Khasanov, A.; Luo, Z.; Guo, Z. Surfactant-Free Synthesized Magnetic Polypropylene Nanocomposites: Rheological, Electrical, Magnetic, and Thermal Properties. *Macromolecules* **2011**, *44*, 4382—4391.

(50) Zhu, J.; He, Q.; Luo, Z.; Khasanov, A.; Li, Y.; Sun, L.; Wang, Q.; Wei, S.; Guo, Z. Property Manipulated Polypropylene-Iron Nano-

composites with Maleic Anhydride Polypropylene. *J. Mater. Chem.* **2012**, *22*, 15928−15938.

(51) He, Q.; Yuan, T.; Zhu, J.; Luo, Z.; Haldolaarachchige, N.; Sun, L.; Khasanov, A.; Li, Y.; Young, D. P.; Wei, S. Magnetic High Density Polyethylene Nanocomposites Reinforced with in-Situ Synthesized Fe@FeO Core-Shell Nanoparticles. *Polymer* **2012**, *53*, 3642−3652.

(52) Coquay, P.; De Grave, E.; Vandenberghe, R. E.; Dauwe, C.; Flahaut, E.; Laurent, C.; Peigney, A.; Rousset, A. Mössbauer Spectroscopy Study of MgAl$_2$O$_4$-Matrix Nanocomposite Powders Containing Carbon Nanotubes and Iron-Based Nanoparticles. *Acta Mater.* **2000**, *48*, 3015−3023.

(53) Vandenberghe, R.; Barrero, C.; Da Costa, G.; Van San, E.; De Grave, E. Mössbauer Characterization of Iron Oxides and (Oxy) Hydroxides: The Present State of the Art. *Hyperfine Interact.* **2000**, *126*, 247−259.

(54) Hanna, S.; Goldanskii, V.; Herber, Rh. Chemical Applications of Mössbauer Spectroscopy. *Science* **1969**, *164*, 939−939.

(55) He, Q.; Yuan, T.; Wei, S.; Haldolaarachchige, N.; Luo, Z.; Young, D. P.; Khasanov, A.; Guo, Z. Morphologyand Phasecontrolled Iron Oxide Nanoparticles Stabilized with Maleic Anhydride Grafted Polypropylene. *Angew. Chem., Int. Ed.* **2012**, *51*, 8842−8845.

(56) Wonterghem, J.; Mørup, S.; Charles, S. W.; Wells, S.; Villadsen, J. Formation of a Metallic Glass by Thermal Decomposition of Fe(CO)$_5$. *Phys. Rev. Lett.* **1985**, *55*, 410−413.

(57) He, Q.; Yuan, T.; Luo, Z.; Haldolaarachchige, N.; Young, D. P.; Wei, S.; Guo, Z. Morphology and Phase Controlled Cobalt Nanostructures in Magnetic Polypropylene Nanocomposites: The Role of Alkyl Chain-Length in Maleic Anhydride Grafted Polypropylene. *Chem. Commun.* **2013**, *49*, 2679−2681.

(58) Sun, S.; Murray, C. Synthesis of Monodisperse Cobalt Nanocrystals and Their Assembly into Magnetic Superlattices. *J. Appl. Phys.* **1999**, *85*, 4325−4330.

(59) He, Q.; Yuan, T.; Zhang, X.; Luo, Z.; Haldolaarachchige, N.; Sun, L.; Young, D. P.; Wei, S.; Guo, Z. Magnetically Soft and Hard Polypropylene/Cobalt Nanocomposites: Role of Maleic Anhydride Grafted Polypropylene. *Macromolecules* **2013**, *46*, 2357−2368.

(60) He, Q.; Yuan, T.; Yan, X.; Ding, D.; Wang, Q.; Luo, Z.; Shen, T. D.; Wei, S.; Cao, D.; Guo, Z. Flame-Retardant Polypropylene/Multiwall Carbon Nanotube Nanocomposites: Effects of Surface Functionalization and Surfactant Molecular Weight. *Macromol. Chem. Phys.* **2014**, *215*, 327−340.

(61) Miles, P.; Westphal, W.; Von Hippel, A. Dielectric Spectroscopy of Ferromagnetic Semiconductors. *Rev. Mod. Phys.* **1957**, *29*, 279−307.

(62) Michielssen, E.; Sajer, J.-M.; Ranjithan, S.; Mittra, R. Design of Lightweight, Broad-Band Microwave Absorbers Using Genetic Algorithms. *IEEE Trans. Microw. Theory Technol.* **1993**, *41*, 1024−1031.

(63) Zhang, X.-J.; Wang, G.-S.; Cao, W.-Q.; Wei, Y.-Z.; Cao, M.-S.; Guo, L. Fabrication of Multi-Functional PVDF/RGO Composites via a Simple Thermal Reduction Process and Their Enhanced Electromagnetic Wave Absorption and Dielectric Properties. *RSC Adv.* **2014**, *4*, 19594−19601.

(64) Lv, R.; Cao, A.; Kang, F.; Wang, W.; Wei, J.; Gu, J.; Wang, K.; Wu, D. Single-Crystalline Permalloy Nanowires in Carbon Nanotubes: Enhanced Encapsulation and Magnetization. *J. Phys. Chem. C* **2007**, *111*, 11475−11479.

(65) Wang, C.; Han, X.; Xu, P.; Wang, J.; Du, Y.; Wang, X.; Qin, W.; Zhang, T. Controlled Synthesis of Hierarchical Nickel and Morphology-Dependent Electromagnetic Properties. *J. Phys. Chem. C* **2010**, *114*, 3196−3203.

(66) Li, N.; Huang, Y.; Du, F.; He, X.; Lin, X.; Gao, H.; Ma, Y.; Li, F.; Chen, Y.; Eklund, P. C. Electromagnetic Interference (Emi) Shielding of Single-Walled Carbon Nanotube Epoxy Composites. *Nano Lett.* **2006**, *6*, 1141−1145.

(67) Kolhatkar, A. G.; Nekrashevich, I.; Litvinov, D.; Willson, R. C.; Lee, T. R. Cubic Silica-Coated and Amine-Functionalized FeCo Nanoparticles with High Saturation Magnetization. *Chem. Mater.* **2013**, *25*, 1092−1097.

(68) Wei, X.-W.; Zhu, G.-X.; Liu, Y.-J.; Ni, Y.-H.; Song, Y.; Xu, Z. Large-Scale Controlled Synthesis of FeCo Nanocubes and Microcages by Wet Chemistry. *Chem. Mater.* **2008**, *20*, 6248−6253.

(69) Li, Y.; Kim, Y. J.; Kim, A. Y.; Lee, K.; Jung, M. H.; Hur, N. H.; Park, K. H.; Seo, W. S. Highly Stable and Magnetically Recyclable Mesoporous Silica Spheres Embedded with Feco/Graphitic Shell Nanocrystals for Supported Catalysts. *Chem. Mater.* **2011**, *23*, 5398−5403.

(70) Wang, L.; Huang, Y.; Sun, X.; Huang, H.; Liu, P.; Zong, M.; Wang, Y. Synthesis and Microwave Absorption Enhancement of Graphene@Fe$_3$O$_4$@SiO$_2$@NiO Nanosheet Hierarchical Structures. *Nanoscale* **2014**, *6*, 3157−3164.

(71) Che, R. C.; Peng, L. M.; Duan, X. F.; Chen, Q.; Liang, X. L. Microwave Absorption Enhancement and Complex Permittivity and Permeability of Fe Encapsulated within Carbon Nanotubes. *Adv. Mater.* **2004**, *16*, 401−405.

(72) Yang, C. Q.; He, Q. Applications of Micro-Scale Combustion Calorimetry to the Studies of Cotton and Nylon Fabrics Treated with Organophosphorus Flame Retardants. *J. Anal. Appl. Pyrolysis* **2011**, *91*, 125−133.

(73) Yang, C. Q.; He, Q. Textile Heat Release Properties Measured by Microscale Combustion Calorimetry: Experimental Repeatability. *Fire Mater.* **2012**, *36*, 127−137.

(74) Babrauskas, V.; Peacock, R. D. Heat Release Rate: The Single Most Important Variable in Fire Hazard. *Fire Safety J.* **1992**, *18*, 255−272.

(75) Wang, X.; Song, L.; Yang, H.; Xing, W.; Lu, H.; Hu, Y. Cobalt Oxide/Graphene Composite for Highly Efficient Co Oxidation and Its Application in Reducing the Fire Hazards of Aliphatic Polyesters. *J. Mater. Chem.* **2012**, *22*, 3426−3431.

(76) Guo, Z.; Park, S.; Hahn, H. T.; Wei, S.; Moldovan, M.; Karki, A. B.; Young, D. P. Magnetic and Electromagnetic Evaluation of the Magnetic Nanoparticle Filled Polyurethane Nanocomposites. *J. Appl. Phys.* **2007**, *101*, 09M511.

(77) Sun, X.; He, J.; Li, G.; Tang, J.; Wang, T.; Guo, Y.; Xue, H. Laminated Magnetic Graphene with Enhanced Electromagnetic Wave Absorption Properties. *J. Mater. Chem. C* **2013**, *1*, 765−777.

(78) Guo, Z.; Lee, S. E.; Kim, H.; Park, S.; Hahn, H.; Karki, A.; Young, D. Fabrication, Characterization and Microwave Properties of Polyurethane Nanocomposites Reinforced with Iron Oxide and Barium Titanate Nanoparticles. *Acta Mater.* **2009**, *57*, 267−277.